Radiochromic film imaging spectroscopy of laser-accelerated proton beams

F. Nürnberg,[1,a)] M. Schollmeier,[1] E. Brambrink,[2] A. Blažević,[3] D. C. Carroll,[4] K. Flippo,[5] D. C. Gautier,[5] M. Geißel,[6] K. Harres,[1] B. M. Hegelich,[5] O. Lundh,[7] K. Markey,[8] P. McKenna,[4] D. Neely,[9] J. Schreiber,[10] and M. Roth[1]

[1]*Institut für Kernphysik, Technische Universität Darmstadt, Schlossgartenstr. 9, 64289 Darmstadt, Germany*
[2]*Laboratoire pour l'Utilisation des Lasers Intenses, Ecole Polytechnique, 91128 Palaiseau, France*
[3]*GSI Helmholtzzentrum für Schwerionenforschung, Planckstr. 1, 64291 Darmstadt, Germany*
[4]*Department of Physics, University of Strathclyde, SUPA, Glasgow G4 0NG, United Kingdom*
[5]*Los Alamos National Laboratory, Los Alamos, New Mexico 87544, USA*
[6]*Sandia National Laboratories, Albuquerque, New Mexico 87185, USA*
[7]*Department of Physics, Lund University, P.O. Box 118, S-22100 Lund, Sweden*
[8]*School of Mathematics and Physics, Queens University Belfast, Belfast BT7 1NN, United Kingdom*
[9]*Rutherford Appleton Laboratory, STFC, Didcot OX11 0QX, United Kingdom*
[10]*Fakultät für Physik, Ludwig-Maximilians-Universität, Am Coulombwall 1, 85748 Garching, Germany*

This article reports on an experimental method to fully reconstruct laser-accelerated proton beam parameters called radiochromic film imaging spectroscopy (RIS). RIS allows for the characterization of proton beams concerning real and virtual source size, envelope- and microdivergence, normalized transverse emittance, phase space, and proton spectrum. This technique requires particular targets and a high resolution proton detector. Therefore thin gold foils with a microgrooved rear side were manufactured and characterized. Calibrated *GafChromic* radiochromic film (RCF) types MD-55, HS, and HD-810 in stack configuration were used as spatial and energy resolved film detectors. The principle of the RCF imaging spectroscopy was demonstrated at four different laser systems. This can be a method to characterize a laser system with respect to its proton-acceleration capability. In addition, an algorithm to calculate the spatial and energy resolved proton distribution has been developed and tested to get a better idea of laser-accelerated proton beams and their energy deposition with respect to further applications. © *2009 American Institute of Physics.* [DOI: 10.1063/1.3086424]

I. INTRODUCTION

Proton acceleration by ultrashort, high-intensity ($I > 10^{18}$ W/cm^2) laser pulses interacting with thin foils has attracted a great deal of attention during recent years and has been widely examined both experimentally and theoretically. The emitted protons reach large particle numbers of up to 10^{13} per pulse with energies in the MeV[1,2] and multi-MeV range.[3–7] These beams have many advantages in comparison to conventionally accelerated proton beams, including low transverse emittance and high brightness as well as short pulse duration.[8–10] For these energetic proton beams various potential applications are proposed, e.g., medical isotope production,[11] proton oncology,[12] proton imaging,[13] injection into conventional accelerators as the next generation proton source or accelerator,[14,15] and as a fast ignitor beam for laser-driven fusion.[16] For these applications, the generation and optimization of proton beams with controllable parameters such as energy spectrum, brightness, and proton energy distribution are essential.

The acceleration of protons during the laser-plasma interaction up to energies above 60 MeV[4,7] is qualitatively described by a plasma expansion model.[17] Relativistic electrons generated by the laser-plasma interaction penetrate through the target foil, escape on the rear side, and form an electron sheath resulting in an electric field of the order of T V/m on the rear surface.[4,5] As the electric field points normal to the target surface, this rear-side accelerating mechanism is called target normal sheath acceleration (TNSA).[18] Atoms at the rear surface, mostly protons present in impurities on the target surface, are field ionized and are accelerated normal to the surface into vacuum along the electric field lines. After the acceleration period [on the order of 1 ps (Ref. 19)], the proton beam is space charge neutral due to comoving electrons. It has been shown that for the laser and target parameters this article deals with, TNSA is the dominant acceleration mechanism.[20,21]

Recently, scaling laws for the TNSA have been published[7,21,22] as well as quasimonoenergetic proton[23] and heavier ion beams.[24] Current research focuses on the optimization of these proton beams for use in a number of applications. For a better understanding of the acceleration mechanism and for controlling the beams it is crucial to have detailed information about the proton beam parameters such as source size, divergence, transverse emittance, and the spatial and energy resolved proton distribution. In this article we

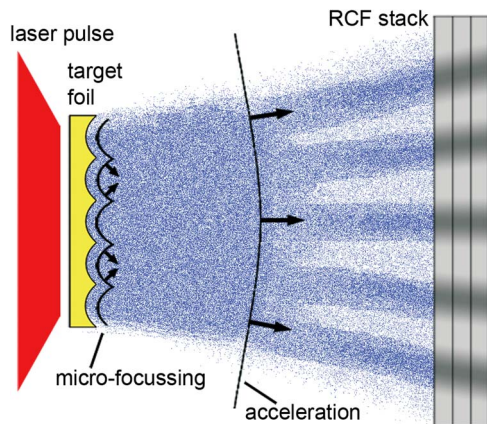a)Electronic mail: f.nuernberg@gsi.de.

FIG. 1. (Color online) Scheme of the foil-induced microfocusing of the laser-accelerated protons. The grooved rear surface of the target foil and the acceleration effect in target normal direction of the TNSA mechanism cause a microfocusing of the protons at the beginning of the acceleration. The separation of these beamlets due to the propagation of the beam is visible in the RCF detector as modulations of the proton density distribution.

FIG. 2. (Color online) Interferometry image of the rear side of a microstructured Au foil with a sine structure with a period of 10 μm and an amplitude of less than 1 μm.

report on a full reconstruction method for laser-accelerated proton beams. Microstructured gold foils were used as target material in combination with calibrated *GafChromic* radiochromic films (RCF) in stack configuration for proton detection and beam parameter determination. An algorithm with the scanned RCFs as input calculates a three-dimensional view of the spatial and energy resolved proton distribution.

II. TOOLS FOR RADIOCHROMIC FILM IMAGING SPECTROSCOPY

With the help of microstructured target foils and film detectors in stack configuration it is possible to specify proton beam parameters resolved in energy with a high spatial resolution. The microcorrugations on the foil rear side generate beamlets in the laser-accelerated proton beam. These perturbations in momentum space of the protons are embedded in the expansion of the beam to a point where the divergence angles originating from different microgrooves are well separated from each other. This is when a contrast pattern or image forms in the RCF detector. This effect is called *microfocusing*,[8,25,26] see schematic diagram in Fig. 1. Therefore the proton beam maps the rear side structure of the foil onto the film detector. Due to deviations of the mapped image in the detector from the ideal image of the inserted grooves in the target, information about the transverse emittance and the source size of the protons can be extracted. The symmetry and the divergence can also be determined by the imprint in the film. By using the RCFs in stack configuration an energy-resolved measurement is possible. Protons with lower energies are stopped in the previous layers, whereas protons with higher energies penetrate through and are stopped in the rear films of the stack. So each RCF can be attributed to an energy bin corresponding to an average proton energy. The fraction of the deposited energy of the penetrating high-energy protons is negligible compared to the main *Bragg*-peak deposition. The energy resolved proton distribution obtained from the film stack completes the beam reconstruction.
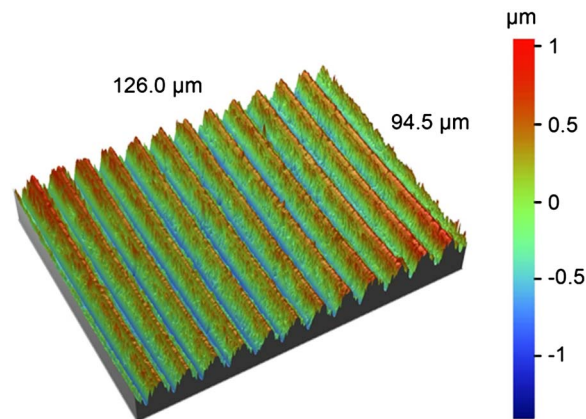
A. Grooved targets

In the last few years different fabrication methods for microstructured foils were tested at the target laboratory of the Technische Universität Darmstadt, Institut für Kernphysik. Structuring by laser ablation, evaporation of a lithographically structured silicon wafer, or direct diamond planning of a thin foil turned out to be too imprecise and extensive. With a microstructured copper wafer (manufactured by the LFM, laboratory for precision machining, Bremen, Germany) delivering the required microstructure with the desired accuracy and using electroplating techniques, microstructured gold foils of different thicknesses could be fabricated. The precision in the distance of the inserted equidistant grooves on the submicrometer scale are a few 100 nm. Figure 2 shows an interferometry image of the grooves on target foil samples. Microstructured gold foils of (5–50) μm thickness with equidistant grooves on the rear surface were produced. The grooves with a line spacing of (3–20) μm have a depth between 1 and 3 μm. Three different groove profiles can be manufactured: a cycloid, an inverse cycloid, and a sine structure.

B. Radiochromic films

For the reconstruction of the laser-accelerated proton beam, it is necessary to have a high-resolution detector to get the spatial-resolved dose distribution of the protons. A common and ideal detector is Gafchromic RCF of the types HD-810, HS, and MD-55.[27] These dosimetry films measure radiation dose, in this case provided by the protons, because their stopping power/range is higher compared to other particles or radiation being generated during the experiment (e.g., heavy ions, electrons, or x rays). After interaction with ionizing radiation the film changes its color from nearly transparent to blue induced by polymerization.[28] The self-developing film has a spatial resolution of more than 10^4 dots per inch (dpi) or less than 2.54 μm according to the manufacturer.

Transmission densitometers, spectrophotometers, or film scanners can be used to digitize the RCFs. Attention should be paid to the time of reading. Nearly complete dyeing of the film (90%) appears within milliseconds. However, during the

first 24 h after irradiation, an increasing dyeing cannot be neglected. It is recommended to read in the films at the earliest of 2 days after exposure, as it was done for the data of this article.

The RCFs have been calibrated for protons by Hey et al.[29] with a microdensitometer. However, we have used the transmission film scanner Microtek ArtixScan 1800f instead of a densitometer to scan larger films faster with the same accuracy. More information about differences in RCF analysis with different scanner types can be found in Refs. 29–31. The scanner calibration was done with a gray scale wedge[32] to convert the raw data into optical density (OD). The films were scanned with a resolution of 500 dpi and a dynamic range of 16 bit gray scales. The same scan parameters were used for both the calibration and the experiment in order to have the same conditions. This scanner could read ODs up to 2.5, the saturation value.

The next step is to convert OD into deposited energy of the protons. This requires a calibration of the sensitive layer of the RCF. During the last few years the chemical composition and also the thickness of the sensitive layer have been changed by the manufacturer. This means that ideally a calibration for each type and production code is necessary. In addition to the effect of the composition difference the data differ from scanner to scanner so that no universal calibration curve for the RCF exists. But the following calibration data could be helpful if the same scanner will be used. The necessary calibration for the RCFs was done at the proton accelerator at the Max-Planck-Institut for nuclear physics in Heidelberg, Germany. The accelerator delivered 8 MeV protons. The deposited energy E_{dep} of the protons (given in keV/mm²) propagating through the film is determined by the SRIM code package[33] and integrated over the volume of the sensitive layer to obtain the total deposited energy.

Figure 3(a) shows the double logarithmic plot of the film calibration curves for the three different film types. As an appropriate approximation for this highly nonlinear slope, an exponential function

$$E_{dep} = \exp\left(\sum_i a_i OD^{b_i}\right) \frac{keV}{mm^2} \tag{1}$$

is suitable to have as a function for further implementation (see Sec. III C). Otherwise a interval spline interpolation is also fine. This approximation is only valid in the OD region of the measured data. For lower ODs of the MD-55 and HS film, it was not possible to achieve measurable data. The shutter closing time of the proton accelerator did not enable measurement of time periods less than 1 s in length, which were necessary for low optical densities. The region with optical densities less than 0.1 was then approximated by a power law $E_{dep} = aOD^b + c$ similar to Refs. 30 and 34. In the range OD > 2.5, the scanner is working within its range of saturation and so the values are not usable. The calibration curves OD versus dose D are shown in Fig. 3(b). Here the different film sensitivities are clearly visible. The dose curve of the insensitive film HD-810 is situated above the more sensitive films MD-55 and HS. For both MD-55 and HS films a lower deposited dose induces the same OD as for type HD-810. So film types MD-55 and HS can be used for
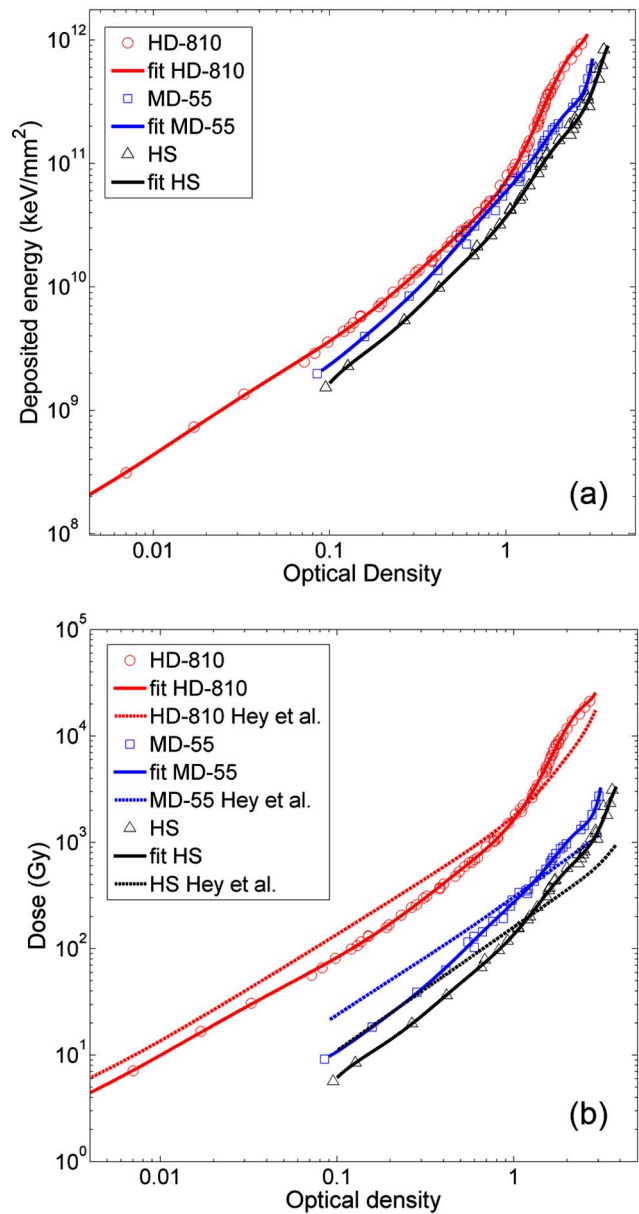

FIG. 3. (Color online) (a) Double logarithmic plots of the proton calibration curves for GafChromic RCF types MD-55, HD-810, and HS. (b) Double logarithmic dose diagram including the calibration curves of Hey et al. (Ref. 29). See Sec. II B of the main text for a discussion of errors.

the detection of lower fluxes as the energy deposition of each particle is higher than in the film type HD-810, equivalent to a darker coloring. The slopes of the dose curves find a good agreement with the calibration in Ref. 29 shown as the dashed lines.

The sources of error for the determination of the OD as well as of the calculation of the deposited energy depend on the accuracy of the delivered beam parameters of the proton accelerator, the film composition, and the measurement. The accuracy of the calibration proton energy from the accelerator is of 0.1%. Beside this, the error of the spot size and the inaccuracy of the current measurement during the calibration can be neglected. The main effect is the inhomogeneity of the beam profile: a uniform irradiation of the film could only be assured within an error of 5%. Another source of error is

given by the accuracy of the scanner of about 3%. The largest error is due to batch-to-batch variations in the film sensitivity of up to 10%.[27] Hence, an overall error of this calibration of 15%–20%, as also published by Hey *et al.*,[29] is an acceptable value for ODs these experiments mostly deal with. Besides the errors for the OD, the inaccuracy of the code SRIM for calculating the deposited energy in the films is on the order of 4%.[33]

III. BEAM RECONSTRUCTION METHOD

In Secs. III A–III E the beam reconstruction method will be described in detail including the definitions of the beam parameters forming the basis of the method and the technique on how to extract the parameters from the measured data.

A. Envelope and microdivergence

As described later in Sec. IV, the stack detector is placed a few centimeters behind the target perpendicular to the target normal direction. A RCF is a two-dimensional detector in space. Therefore, a transverse cross section of the proton beam profile will be visible on the film. With its size and the distance between target and detector, it is possible to determine an envelope-divergence angle α of the proton beam. A second divergence dimension also well known in accelerator physics is the microdivergence $\Delta\alpha$. This can be measured using either the pepper-pot method[35] or transverse slit scanners,[36] a more comparable technique to microgrooved targets discussed later. The microdivergence characterizes the broadening of the particle trajectories and is important for the emittance calculation (see Sec. III C). By using microgrooved targets, the microdivergence can be estimated by measuring the line width of a groove mapped in the RCF detector. An energy resolved measurement can be made by using RCFs in stack configuration instead of a single film. High energy protons penetrate through the first films and will be fully stopped in the later films of the stack. Therefore, each film layer can be attributed to a certain proton energy.

B. Real and virtual source size

By counting the line pattern in each RCF and by multiplying with the original line space of the microstructured foil, the energy resolved real source size S_{real}, i.e., the proton emission zone on the target rear surface, can be determined. To get quantitative information about the quality of laser-accelerated proton beams, the virtual source size S_{virtual} is more suitable, the point source where the protons appear to originate. The virtual source size can be determined by extrapolation of the proton trajectories to a region in front of the target.[37] With the well known microstructure in the target and the measured line pattern in the RCFs, the necessary data set is available for the extrapolation. The width of the virtual source size is a suitable parameter for comparison of beam quality between different proton beams.

C. Transverse emittance

Another important parameter is the transverse emittance ϵ of an ion beam. Much of accelerator physics centers on

understanding the evolution of beam particles in four-dimensional x-x' and y-y' phase space (beam propagates in the z-direction). Typically, restricted two-dimensional phase-space projections in x-x' and/or y-y' are analyzed to simplify interpretations, and here, because of the circular symmetry of laser accelerated proton beams, one dimension is sufficient. In the following discussion the beam emittance in the plane perpendicular to the microstructure in the target rear surface will be determined for a specific proton energy. In view of the nature of the source, there is always a spread in kinetic energy and velocity in a particle beam. Each point on the surface of the source emits protons with different initial magnitude and direction of the velocity vector. The emittance provides a figure of merit for describing the quality of the beam. Each proton represents a point in the x-x' phase space. Herein, a laminar beam of charged particles is displayed by a line of vanishing thickness.[35] Deviations from laminarity due to a transverse temperature of the beam results in a blurring of the transverse phase space. The definition of the transverse emittance ϵ in the space-divergence phase space is the ellipse of minimum area defined by the proton beam divided by π,

$$\epsilon_{\text{ellipse}} = \frac{1}{\pi} \int \int \mathrm{d}x\mathrm{d}x', \tag{2}$$

in units of π mm mrad. This emittance is also called total or 100% emittance. The size of the emittance can be given as the ellipse enclosing the distribution (practical quantity) or as root-mean-square (rms) emittance (statistical quantity)[38]

$$\epsilon_{\text{rms}} = \sqrt{\langle x^2\rangle\langle x'^2\rangle - \langle xx'\rangle^2}, \tag{3}$$

with the second moment in the particle coordinate x (y can substitute for x as symmetry is assumed) defined by

$$\langle x^2\rangle = \frac{\int x^2 f(x,x')dxdx'}{\int f(x,x')dxdx'} \tag{4}$$

$$\Rightarrow \frac{\sum_i a(x_i)b(x_i')x_i^2\Delta x_i\Delta x_i'}{\sum_i a(x_i)b(x_i')\Delta x_i\Delta x_i'}. \tag{5}$$

In a similar fashion the other second moments $\langle x'^2\rangle$ and $\langle xx'\rangle$ are defined. a and b are the weighting factors of the beam intensity. For the measurements of laser-accelerated proton beams a and b are equal 1. For a uniform beam distribution the relation between the two quantities is $\epsilon_{\text{ellipse}} = 4\epsilon_{\text{rms}}$.

Unfortunately, there is no global definition of emittance that is consistently used in accelerator and ion beam physics, a fact that often causes confusion when results and publications are compared. The definition can involve a phase space area, divided by π or not, or the rms emittance or only an area including a fraction of the whole beam. In this article we will use two different approaches. First the emittance is calculated by the ellipse definition including nearly 100% of the proton beam, and second the rms emittance is determined by using the measured data to average the whole particle distribution.

The emittance, as defined here, depends on the kinetic energy of the protons (see Ref 39). According to Liouville's theorem, the emittance does not remain constant for different proton energies. The emittance change is inversely proportional to the relativistic parameters γ and β. Geometrically this corresponds to an increase/decrease in the slope x' (and hence the area in x-x' phase space) as the longitudinal momentum p_z changes. To compare the beam quality of protons with different energy, the normalized emittance is introduced,

$$\epsilon_{\text{norm}} = \beta\gamma\epsilon, \tag{6}$$

with $\gamma = 1 + E_{\text{prot}}/E_{0,\text{prot}}$ and $\beta = \sqrt{1 - 1/\gamma^2}$, where E_{prot} is the proton energy and $E_{0,\text{prot}} = 981$ MeV is the proton rest energy. The normalized transverse emittance $\epsilon_{\text{trans,norm}}$ is a well known parameter in accelerator physics because it is constant during acceleration and a comparison of emittance values in different acceleration phases (different proton energies) is possible. However, it is a lot easier to compare the normalized values to values of conventional accelerators.

A useful fit for the normalized transverse emittance is the parallelogram approximation of the ellipse in phase space. In doing so Eqs. (2) and (6) pass into

$$\epsilon_{\text{real}} \approx (\beta\gamma)S_{\text{real}} \cdot \Delta\alpha \tag{7}$$

with the real source size S_{real} and the microdivergence $\Delta\alpha$ of the proton trajectories. The error of this area approximation is $A_{\text{ellipse}}/A_{\text{parallelogram}} = (\pi ab)/(2a2b) = \pi/4 \rightarrow 27\%$ with the semiaxis a and b of the ellipse.

Another possibility to determine the transverse beam emittance is by using the virtual source size. According to Liouville's theorem, the emittance for one proton energy remains constant independent of the position of the measurement. Due to extrapolation inaccuracies the position of the lines within the virtual source size cannot accurately be identified. The extrapolated trajectories cross, so the full divergence angle is an upper estimation and Eq. (7) changes to

$$\epsilon_{\text{virtual}} \approx (\beta\gamma)S_{\text{virtual}}\alpha. \tag{8}$$

D. Deconvolved proton spectrum

The RCF detector in stack configuration enables measurement of the energy spectrum of a laser accelerated proton beam. Protons penetrating through RCF lose kinetic energy in the film material, besides charge transfer and scattering of the protons. This is described by the differential energy loss dE_{prot}/dx. The deposited energy per proton in the active layer is plotted in Fig. 4 for the first three HD-810 films (red lines). The energy of the maxima of these curves corresponds to the energy of the protons, which are totally stopped in the sensitive layer (Bragg peak). Because of the thicker sensitive layers, the maxima of the energy deposition of the MD-55 and HS films are higher than for HD-810. For the film type MD-55 with two sensitive layers the resulting energy deposition curve is an overlap of two shifted curves. Hence, this energy deposition curve has two maxima. Besides the deposition curves the necessary film data were digitized by reading in the RCFs with the same scanner parameters as used for the calibration. After the subtraction of the
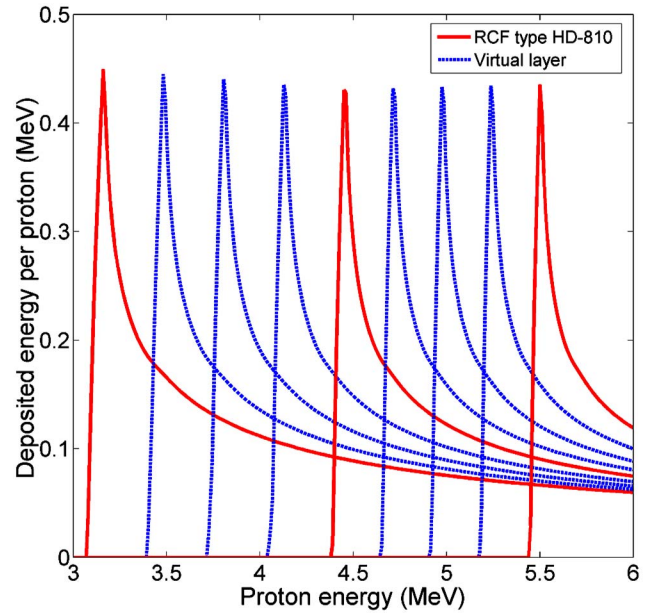

FIG. 4. (Color online) Energy deposition curves for three HD-810 films (red solid lines). The blue dashed curves are virtually inserted layers for the proton distribution reconstruction (see Sec. IV F).

radiation background (HD-810: OD=0.05, MD-55: OD=0.2, HS: OD=0.24), the proton beam envelope was extracted. A threshold limit for the beam boundary in the RCF was chosen to minimize the influence of the perturbations in the outer regions. Outsized impurities such as dust or scratches in the spot can be marked and removed with an additional filter.

Protons deposit a fraction of their energy in all layers penetrating through before being stopped, see Fig. 4, so the measured total deposited energy E_{total} in a specific RCF is the convolution of the spectrum with the response function of the RCF,

$$E_{\text{total}} = \int \frac{dN(E')}{dE} E_{\text{loss}}(E')dE', \tag{9}$$

where dN/dE is the particle number spectrum per unit energy and E_{loss} is the calculated energy loss of a proton with energy E in the given layer. This fact requires each layer to be deconvolved by the nonlinear detector response function to determine the particle spectrum dN/dE. Hence, it requires a deconvolution to get the particle number spectrum.

The way it was been done in this publication is inverse—a convolution with an assumed function for the proton spectrum. Recent publications as well as Thomson Parabola data show an exponential behavior of the proton spectrum. There are still different types used, e.g., a simple exponential decay as a Boltzmann distribution for a thermal plasma expansion, Eq. (10), a modified exponential by Fuchs et al.[40] as a result of an isothermal, quasineutral plasma expansion, Eq. (11),[41] or a Gaussian including an adiabatic plasma expansion,[42] Eq. (12),

$$\frac{dN}{dE} = \frac{N_0}{E}\exp\left(-\frac{E}{k_BT}\right), \tag{10}$$

TABLE I. Laser and target parameters for the different laser systems.

Laser system	E_{laser} (J)	τ_{laser} (fs)	λ_{laser} (nm)	Incidence (deg)	Focus (μm)	I_{laser} (W/cm^2)	d_{target} (μm)	Groove depth, separation (μm)
PHELIX	3.8	580	1054	45	8	1.3×10^{19}	30	1, 3
TRIDENT	18.7	600	1054	44	14	2×10^{19}	10	1, 3
100TW-LULI	15.4	350	1057	0	8	5.6×10^{19}	50	1, 5
VULCAN	125.3	1000	1053	5	5	3.5×10^{20}	25	1, 10

$$\frac{dN}{dE} = \frac{N_0}{\sqrt{2Ek_BT}}\exp\left(-\sqrt{\frac{2E}{k_BT}}\right), \tag{11}$$

$$\frac{dN}{dE} = \frac{N_0}{E}\exp\left[-\left(\frac{E}{k_BT}\right)^2\right]. \tag{12}$$

With the function for the proton spectrum and the E_{loss} values given by SRIM a theoretical total deposited energy is calculated for each RCF layer in the stack. The integral in Eq. (9) is solved by Simpson's rule for numerical integration. The calculated energy values of the RCFs are compared to the experiment. By minimization of the rms deviation, the parameters N_0 and k_BT are iteratively determined.

E. Spatial and energy resolved proton spectrum

In comparison to standard particle spectrometers, as e.g., magnetic spectrometers,[43,44] RCFs can measure the full proton distribution not only energy resolved but also spatially resolved. Hence, a three-dimensional (x, y, E) proton distribution of the beam can be obtained. In this article we present an algorithm to determine the proton distribution resolved both spatially and in energy. This is because the spatial information of a certain energy is of interest for many applications. To improve the energy resolution, we introduced further virtual RCF layers by interpolating between the existing layers (shown as the blue lines in Fig. 4). The graphical deconvolution is done by a weighted subtraction of all films from each other. Thus we obtain the spatial intensity distribution for each layer. To obtain particle numbers from the deposited energy an integration over the spectrum fit function is carried out. The algorithm will be described in detail with an example in Sec. IV F.

IV. EXPERIMENTAL TEST OF RIS

Experiments were performed at four different laser systems: the PHELIX laser system at Gesellschaft für Schwerionenforschung, Darmstadt (GSI), the TRIDENT short-pulse laser at the Los Alamos National Laboratory (LANL), the 100 TW laser system at the Laboratoire pour l'Utilization des Lasers Intenses (LULI), and the VULCAN Petawatt laser at the Central Laser Facility, Rutherford Appleton Laboratory. The laser system parameters are listed in Table I. The pulses were focused onto thin microstructured gold foils at different incident angles with respect to the target normal. At TRIDENT and 100TW-LULI a prepulse of amplified spontaneous emission (ASE) was present 0.5 ns before the main pulse at a contrast ratio (prepulse to main pulse) of 10^{-6}; for PHELIX the prepulse was minimized to 1 ns with a ratio of 10^{-5}. At VULCAN a plasma mirror[45] was positioned in the focusing beam to suppress the intensity of the ASE to less than 10^{11} W/cm^2 (contrast ratio $<10^{-9}$, reflectivity 32%). For all laser systems the full width at half maximum (FWHM) of the focal spot contains $\sim$50% of the laser energy. The targets for the experiments were of (10–50) μm thick gold foils with equidistant grooves on the nonirradiated rear surface. The grooves with a line spacing of (3–10) μm had a depth less than 1 μm. For the proton beam diagnostic a stack of calibrated RCFs was used, placed 30–50 mm behind the target.

For TRIDENT, 100TW-LULI, and VULCAN, three different RCF stack configurations were used, i.e., different sequences of film types HD-810 and MD-55. For example, the TRIDENT stack consisted of 19 RCFs type HD-810 and three of type MD-55 (see Fig. 5). Since during the laser-target interaction when parasitic radiation was created, the RCF stacks were wrapped in 12.5 μm (TRIDENT), 25.4 μm (100TW-LULI), or 13 μm (VULCAN) thick Al
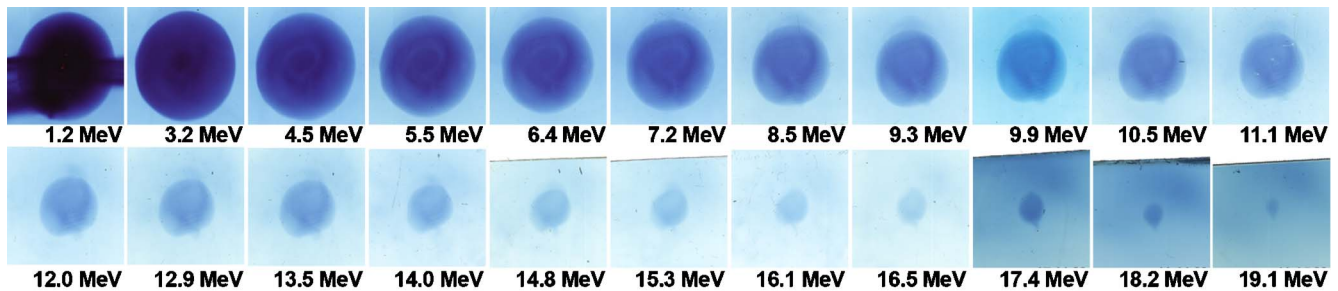

FIG. 5. (Color online) RCF stack of the TRIDENT experiment: 19 films of type HD-810 and three films of type MD-55. There was no signal in the following six MD-55 films of the stack. Below each film the proton Bragg peak energy is given.
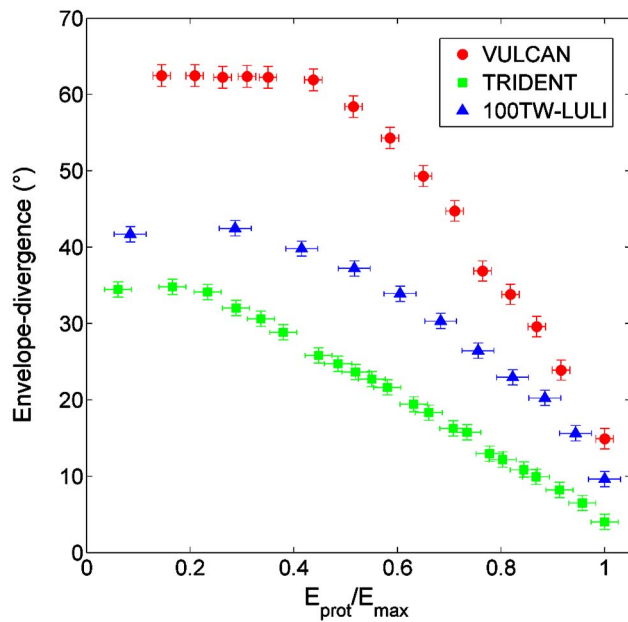
FIG. 6. (Color online) The full envelope divergence scaled to the maximum proton energy for each shot (VULCAN $E_{max}=29.7$ MeV, TRIDENT $E_{max}=19$ MeV, 100TW-LULI $E_{max}=16.2$ MeV). For increasing proton energies the divergence decreases.

foil for shielding. To calculate the characteristic energy for the stopped protons in a specific film of the RCF stacks, the deposited energy values of the SRIM code package are used and summed for the particular sensitive layer. Accelerated protons with this calculated proton energy are fully stopped in this sensitive layer (see energy values in the corner of each image, Fig. 5). In the PHELIX experiment no proton signal in the RCF stack was visible. Since in this experiment only the preamplifiers were used, the proton energies were so low that the energy was fully deposited in the 17.8 μm thick Al shielding foil ($E_p < 1.2$ MeV), so the stack detector was re-placed with CR-39, a solid state nuclear track detector.[46] Since this detector is not sensitive to parasitic radiation, the Al foil could be removed for the detection of the low energy protons.

The combination of microstructured target foils and RCF detectors enables the energy resolved measurement of the envelope and microdivergence, the real and virtual source sizes, and the transverse emittance of the proton beam within a single experiment. Additionally, the deconvolved proton spectrum as well as the spatial and energy resolved proton distribution can be extracted. In this section, respectively, one shot of each laser system will be discussed.

A. Envelope and microdivergence

With the given distance between target and RCF as well as the measurement of the size of the proton beam in the RCF, the energy resolved envelope-divergence α of the protons can be determined, as shown in Fig. 6. The proton energies are scaled to the maximum proton energy for each shot (VULCAN $E_{max}=29.7$ MeV, TRIDENT $E_{max}=19$ MeV, 100TW-LULI $E_{max}=16.2$ MeV). For small pro-ton energies the angle of beam spread is nearly constant, but

TABLE II. Energy resolved source size and divergence values for four different laser systems: real source size S_{real}, virtual source size $S_{virtual}$, position of $S_{virtual}$ in front of the target, microdivergence $\Delta\alpha$, and envelope-divergence α of the proton beam.

Laser system	E_{prot} (MeV)	S_{real} (μm)	$S_{virtual}$ (μm)	Position in front of the target (μm)	$\Delta\alpha$ (mrad)	α (mrad)
PHELIX	<1.2	57	4.0	61	12.5	585
TRIDENT	6.4	69	4.0	125	6.7	475
	9.9	42	1.0	112	8.3	335
	13.5	24	0.9	87	10.0	238
100TW-LULI	4.7	85	5.4	75	5.3	616
	9.8	45	1.4	31	7.4	531
	13.3	25	0.4	31	7.9	303
VULCAN	6.2	500	12.1	372	10.3	1057
	17.4	220	11.0	173	20.5	853

for increasing energy the angle decreases approximately linear/parabolic.

The microdivergence $\Delta\alpha$ is defined by the spread of the proton trajectories given by the deviation of the proton tra-jectories from the ideal. The grooved target rear side effects a microfocusing of the proton beam. This perbutation in the beam distribution is visible in a line pattern in the RCF de-tector. For increasing proton energy the microdivergence in-creases, see Table II. This clearly shows the temperature ef-fect of the proton beam. The microdivergence is comparable with the thermal spread of the beam.

B. Real and virtual source size

Figure 7 shows a RCF example with the visible lines and the energy resolved real source sizes for all laser systems. For increasing proton energies the real source size of the protons fits a Lorentzian shape. The highest energy protons
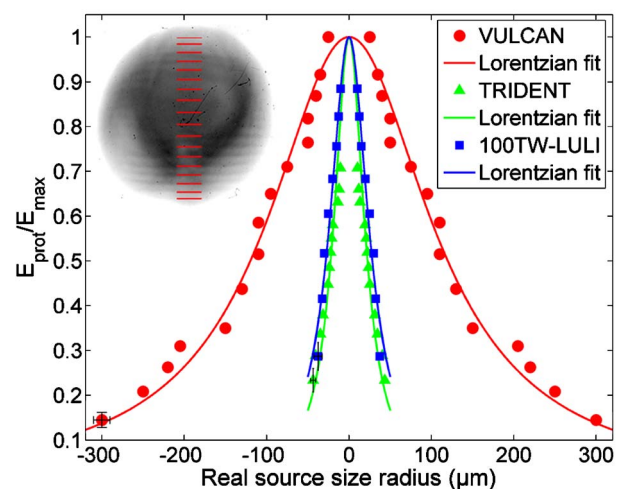

FIG. 7. (Color online) Energy resolved, real source size of the laser-accelerated proton beams. The energies are normalized to the maximum proton energy of each shot. A Lorentzian fit (line) can be applied with a FWHM of 240 μm for VULCAN, 44 μm for TRIDENT, and 56 μm for 100TW-LULI. Inset: intensity modulation in a RCF for $E_{prot}>8.5$ MeV. The positions of the imprinted lines are marked in red. For the measurement error of the line counting to estimate the source size of the proton beam a double line spacing is sufficient: TRIDENT 6 μm, 100TW-LULI 10 μm, VULCAN 20 μm. See example error bars for the lower left data points.
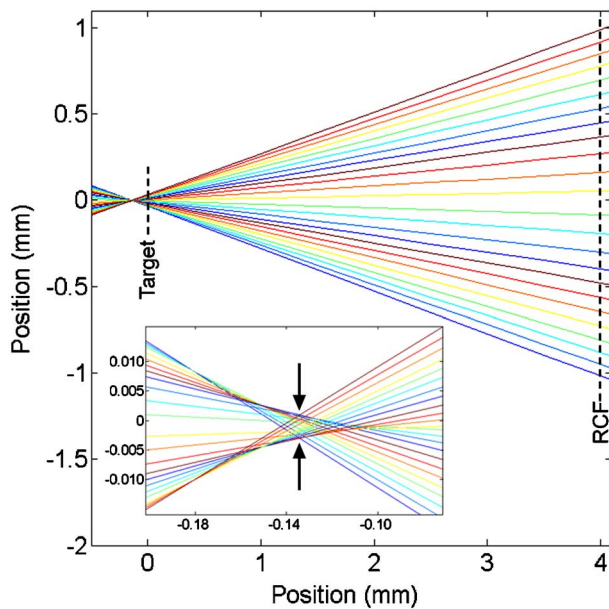
FIG. 8. (Color online) Extrapolation for the virtual source size. Each color pair corresponds to one line in the detector and one groove on the target rear side. The position of the target rear side is at the abscissa value $x=0$. The embedded figure is a blow up of the virtual source size region. For the TRIDENT shot in this figure (6.4 MeV protons) the virtual source size extension defined by the envelope is about 4 μm.

are accelerated in the center. This fits nicely to a bell-shaped distribution of the electrons in the sheath responsible for the proton acceleration.[8] Because of the low contrast of the lines, it was not possible to resolve the source size for the highest proton energies for TRIDENT and 100TW-LULI. The source size for the PHELIX shot is (57 ± 3) μm for protons with energies <1.2 MeV.

For a perfect laminar, straight beam expansion, an extrapolation of the proton trajectories to the region in front of the target resulting in a point source should be possible (linear extrapolation across the line in the detector and the groove in the target). Figure 8 shows that such an extrapolation to a point source for laser-accelerated proton beams is not possible. In addition, the trajectories cross, so the virtual source size S_{virtual} is the waist diameter of the envelope of the extrapolated trajectories. For the extrapolation in Fig. 8 the virtual source size is 4 μm. The calculated values for the four analyzed shots can be found in Table II including the position of S_{virtual} in front of the target. For increasing proton energies the virtual source size decreases as well as the position in front of the target. From Table II it is deduced that the calculated source size values for the PHELIX, TRIDENT, and 100TW-LULI laser systems are in the same band, only the VULCAN Petawatt system is an outlier. However, the VULCAN values fit with previous published data[47] concerning virtual source size and position.

C. Transverse emittance

As mentioned above the evolution of the beam particles is described by the x-x' phase space. The behavior is different if linear or nonlinear forces act on the protons. When forces are linear, particles tend to move on ellipses of constant area. The whole particle distribution can be described
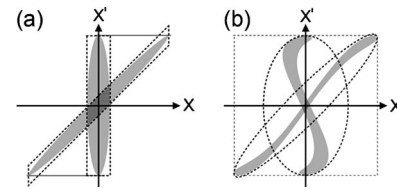

FIG. 9. Schemes of particle beams affected by different forces. (a) The whole particle distribution can be described by an ellipse of minimum area including the proton beam. At the origin, it is in the vertical direction; during expansion the ellipse will be elongated/shrinked and rotate. The dashed parallelograms show the approximation of the ellipse area. (b) Nonlinear force components distort orbits and cause undesirable effects. The transverse emittance increases and parallelogram approximations yield in incorrect results.

by an ellipse of minimum area including the proton beam, see Fig. 9(a). At the source origin, the ellipse is in the vertical direction; during expansion the ellipse will become sheared. The envelope-divergence x' is the same, the beam diameter x increases, but the area of the ellipse is still conserved according to Liouville's theorem. The dashed parallelograms show the approximation of the ellipse area to calculate the transverse emittance after Eq. (7). Nonlinear force components distort orbits and cause undesirable effects, as shown in Fig. 9(b). The gray area is not an ellipse anymore. So the effective phase space area grows (dashed ellipse). There are elements in accelerator physics to compensate this effect, but only on small scales. The acceptance of an accelerator limits the size of the area in phase space. If particles are located in larger areas they will disappear in the accelerator. Nevertheless, the gray area is still conserved. In this case, it is not possible to calculate the transverse emittance using Eq. (7). This area does not reflect the effective emittance area and results in a misleading value. Because of the crossing trajectories at the position of the virtual source size, the correct way to get an upper approximation is with the parallelogram method in Eq. (8), although this method is very inaccurate, as pointed out by the large, gray dashed parallelogram in Fig. 9(b).

Figure 10 shows the x-x' phase space of the TRIDENT proton beam at two different positions, one at the position of the virtual source size (a) and the second at the target rear side (b). The nonlinear effects of the laser-accelerated proton beams can be seen in Fig. 10(a). The extrapolated data show a kind of a S-shaped behavior in phase space highlighted by the dashed connecting lines of the data points. The counterclockwise rotation of the phase space ellipse for increasing proton energy is a characteristic that can also be seen in simulations.[19] For higher proton energies the S-shaped distortion on the data decreases and the effective emittance decreases as well. Both parallelogram approximations do not work because the resulting area does not fit the calculated dashed ellipse. The phase space at the target rear side [see Fig. 10(b)] is the sheared version of the original phase space in Fig. 10(a). The source size is now much larger because of the expansion of the divergent proton beam. The data points are the values given by the microstructured surface and the line pattern in the detector. For large x' the aberration from the linear behavior (dashed straight lines) due to the nonlinear force is still visible and increases the effective emittance
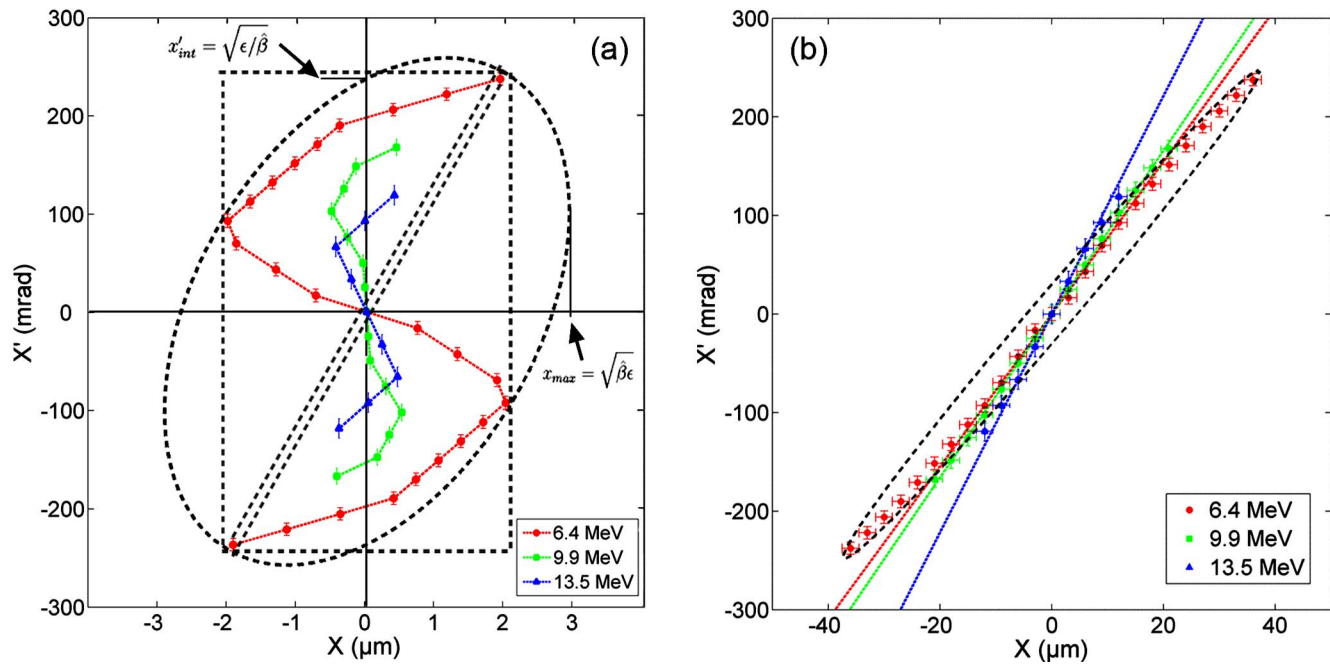
FIG. 10. (Color online) (a) Phase space of the TRIDENT beam at the position of the virtual source size for three different proton energies. The S form resulting from nonlinear forces increases the size of the ellipse. In this case the dashed parallelogram approximation for the phase space area is completely misleading. The correct way is to use the ellipse projections x'_{int} and x_{max}. (b) Real source size position vs divergence. The dashed, straight lines correspond to laminar beams where only linear forces exist. The aberration, as well as the energy dependent counterclockwise rotation of the phase space, is visible. The dashed ellipse is fitted to the experimental data to calculate the emittance.

illustrated by the dashed ellipse in phase space.

Both data sets have shown that the area approximation by a parallelogram is not a feasible method to calculate the transverse emittance. To calculate the area $A_{ellipse}$ of the ellipse the semimajor and semiminor axes have to be determined. By projecting the ellipse onto the x axis, the values for the semiaxes can be read off the coordinate axes,[39]

$$\epsilon = x_{max} x'_{int} = \sqrt{\hat{\beta}\epsilon}\sqrt{\epsilon/\hat{\beta}}, \tag{13}$$

where $\hat{\beta}$ is a Twiss parameter of the Courant–Snyder formulation. The rms emittance defined by Eq. (3) can directly be estimated with measured data and the discretized second moments according to Eq. (5). For a more precise statistical value, virtual data points were extrapolated. More data on the dashed connecting line in Fig. 10(b) do not change the emittance, only the transverse/angular behavior. Here, two attitudes of the phase space of laser-accelerated proton beams have to be considered to scale the value of the extrapolated data points. The line pattern intensity over the whole RCF image is more or less a flat top in the center and decreases linearly in the boundary area to 50% of the flat-top intensity. Beside the change in beam intensity the line pattern profile is important for the transverse extrapolation. A lineout yields to a parabolic intensity profile of a line pattern with decreasing intensity to 10% of the peak value.

All calculated values for the normalized, transverse emittance in units of π mm mrad are summarized in Table III. The reason for the decrease in emittance for all laser systems (ellipse as well as rms method), except VULCAN, is the energy dependent decrease in the source size. The difference in $\epsilon_{real,ellipse}$ and $\epsilon_{virt,ellipse}$ is due to different effective emittances. It is the best possible ellipse approximation of

the data to compare it with acceptances of accelerators and not the real occupied area of the protons in phase space. By comparing $\epsilon_{ellipse}$ and $4 \times \epsilon_{rms}$ the emittances match in the order of magnitude. But the measured laser-accelerated proton beams still show divergences from the uniform case. A main reason, therefore, could be the nonlinear forces and their effect on the phase space because uniform beams are characterized by the six-dimensional phase space.

The $\epsilon_{ellipse}$ values are a rough approximation (upper limit) for the emittance. But considering the nonlinear effects in phase space it was not possible to reach values on the order of $10^{-3}\pi$ mm mrad already found by Cowan et al.[8] In comparison to conventional accelerators as the GSI UNILAC $[\epsilon = (5-10)\pi$ mm mrad (Ref. 48)], the transverse emittance

TABLE III. Normalized, transverse emittance in unit of π mm mrad at two positions: at the position of the virtual and the real source size. The rms and the ellipse method were used to estimate the area in phase space. For uniform beam distributions $\epsilon_{ellipse}$ is $4 \times \epsilon_{rms}$. The tabulated emittances match in the order of magnitude but laser-accelerated proton beams still show divergences from the uniform case.

	E_{prot} (MeV)	$\epsilon_{virt,ellipse}$	$4 \times \epsilon_{virt,rms}$	$\epsilon_{real,ellipse}$	$4 \times \epsilon_{real,rms}$
PHELIX	1.2	0.0624	0.0187	0.0436	0.0803
TRIDENT	6.4	0.0825	0.0347	0.1563	0.1732
	9.9	0.0229	0.0193	0.0933	0.0689
	13.5	0.0164	0.0172	0.0627	0.0360
100TW-LULI	4.7	1.4570	0.0614	0.3118	0.3119
	9.8	0.6528	0.0681	0.1446	0.1533
	13.3	0.0104	0.0475	0.0809	0.0277
VULCAN	6.2	0.3606	0.1396	1.2766	2.0342
	17.4	0.9374	0.2278	0.1667	1.0919

of laser accelerated proton beams is one to two orders of magnitude lower, and compared to the HIT ECR source [$\epsilon = (150-300)\pi$ mm mrad (Ref. 49)] is even more. This better laminarity is one of the major advantages of these beams for further applications such as focusing. The minimum focal spot of a given beam is determined by the emittance.

D. Possible sources of error

The inaccuracy of the measurement is given by the contrast of the line pattern in the RCFs, especially in the outer region of the spot. The grooves of the microstructured target foils are very homogeneous. The line distances of 3 μm for the TRIDENT foils, 5 μm for the 100TW-LULI foils, and 10 μm for the VULCAN foils as well as the line depth of 1 μm were characterized with a scanning electron microscope. The discrepancies average out at 200 nm. The error of the source size determination is mainly due to the error in line counting, thus it is estimated to be double groove distance. The extrapolation to estimate the virtual source size and position depends mainly on the accuracy of reading the position of the line pattern in the RCF. Different calculations yield to a mean error of 20%. The smooth boundary of the beam spot and the noncircular form make it difficult to determine the angle of beam spread. However, this error is only on the order of some percent. The values presented here are due to the ellipse fitting only an upper limit for the emittance. But these values are fine enough to compare them with existing limits for accelerator acceptances concerning future injection of laser-accelerated proton beams as a new kind of particle source.

E. Deconvolved proton spectrum

The Gaussian particle number spectrum [see Eq. (12)] was proved and tested for proton beams of the TRIDENT laser system, here as an example. With the function for the proton spectrum and the E_{loss} values given by SRIM a theoretical total deposited energy is calculated for each RCF layer in the stack (red line in Fig. 11). By minimization of the rms deviation between the calculated energy values of the RCFs and the theoretical total deposited energy, the parameters N_0 and $k_B T$ were iteratively determined. For the example of the TRIDENT laser system, the fit parameters are $N_0 = 3.50 \times 10^{11}$ and $k_B T = 8.74$ MeV.

F. Spatial and energy resolved proton spectrum

With the same proton beam example of the TRIDENT laser system (see Fig. 5) the above described algorithm (Sec. III E) is used to determine the proton energy spectrum, as well as resolving spatially, and will be explained in detail. The beam was detected with a RCF stack consisting of 19 HD and 3 MD films. The first RCF is neglected in all calculations because debris and heavy ions do not enable unambiguous identification of the proton signal. The mean energy interval between two RCFs is 850 keV. The interval size is decreased by inserting virtual active layers for a better energy resolution. The interpolation between the values of the angle of beam spread (Fig. 6) enables determination of the correct spot radius for the proton energy position for which a
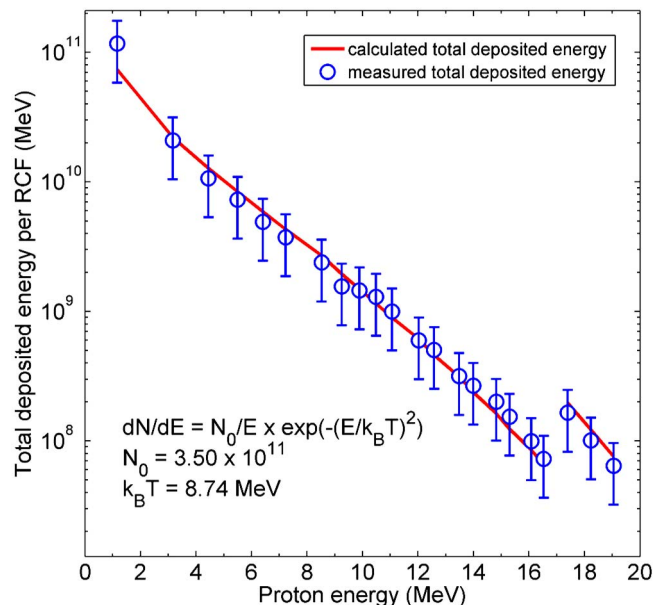

FIG. 11. (Color online) Comparison of the calculated total deposited energy values of the RCFs and the experiment at TRIDENT. By minimization of the rms deviation, the parameters N_0 and $k_B T$ are iteratively estimated as given in the figure. The last three values are lying above the trend of the other films because they are of the more sensitive film type MD-55.

new layer is inserted. Then this spot size is cut out of the previous layer and is placed at the new position. On the basis of the deposited energy in all RCFs (Fig. 11) and the interpolation between these measured values the deposited energy of the inserted layer can be matched. Due to a computational limit only three new virtual layers were inserted between two given RCFs. The resulting stack was then of the size of 81 layers and the mean energy interval decreased to 198 keV.

A weighted subtraction of all films from each other is the way to include the graphical deconvolution of the proton energies. All following layers have to be subtracted from the former layer to deduct the different amounts of deposited energy from higher proton energies in a given film. The weighting factors for a specific stack layer (specific proton energy) are calculated, as shown in Fig. 12, with the help of the energy deposition curves (Fig. 4). Protons with the energy E_{Bragg} are stopped in the corresponding RCF and deposit the energy $E_{dep,max} = E_{dep}(E_{Bragg})$. These protons also lose kinetic energy in each of the previous layers X such that $E_{dep,X} < E_{dep,max}$, so the weighting factors for the previous layers X are the ratios of $E_{dep,X}$ and $E_{dep,max}$.

Because the spatial intensity profile of the proton beam accelerated using Trident is round, a cylindrical symmetry can be assumed. Figure 13(a) shows a cut through the three-dimensional view of the TRIDENT energy deposition after the graphical deconvolution. The color values correspond to deposited energy per mm² of the RCF. Here, in comparison to Thomson parabola spectrometers, the solid angle depends on the position in the RCF. The difference in film sensitivity is clearly visible for proton energies higher than 17 MeV. Above this energy the more sensitive film type MD-55 was placed. The thicker sensitive layer results in a higher energy deposition.
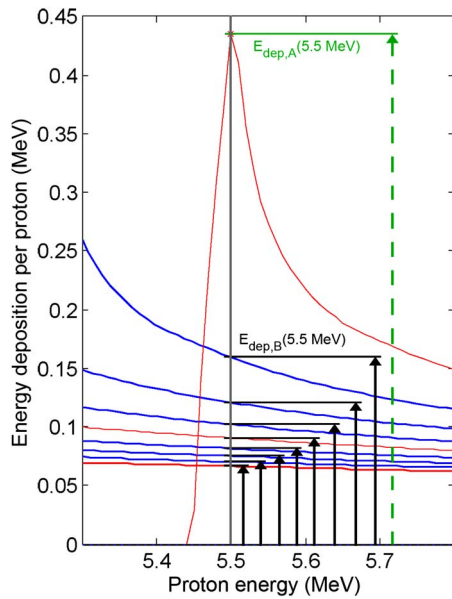
With the described subtraction we are able to extract an

FIG. 12. (Color online) Weighting factors for the graphical deconvolution for the proton energy of $E_A = 5.5$ MeV (blow up of the right red curve in Fig. 4). If the layer A is subtracted from the layer in front of it (B) with $E_B < E_A$, the total deposited energy distribution has to be weighted with the factor $E_{dep,B}(5.5 \text{ MeV})/E_{dep,A}(5.5 \text{ MeV})$, the ratio of the deposited proton energy of 5.5 MeV protons in the previous layer B, the maximum deposited proton energy in layer A, and so on.

angular resolved spectral distribution of the proton beam. The surface plot in Fig. 13(b) shows the result of this calculation for the TRIDENT beam. Due to the weighted subtraction, a ring structure in the deconvolved RCF image is not observed, in contrast to the results by Breschi *et al.*[50] Figure 13(b) shows a quite good flat-top profile of the beam.

Due to the decrease in the energy interval between two layers and the deconvolution by the subtraction, a proton number per layer can be estimated. Therefore, the summarized deposited energy of a layer is divided by the deposited energy of one proton with its Bragg peak located in this

layer. The comparison of these values and the proton distribution function obtained by the analytical deconvolution (Sec. IV E) is shown in Fig. 14. The proton number is given for an energy interval of 200 keV. This size is consistent with the energy interval between two layers in the graphical subtraction. The agreement of the measurement and the fit confirms the use of a Maxwellian proton distribution as a feasible approximation for the spectrum.

V. CONCLUSION

We reported on laser-proton-beam acceleration from thin microstructured gold foils detected by RCFs in stack configuration. With this setup it is possible to fully reconstruct laser-accelerated proton beams concerning real and virtual source size, angle of beam spread, transverse emittance, and spatial and energy resolved proton distribution, respectively. For this purpose microstructured gold foils were manufactured and characterized and three different RCF types MD-55, HS, and HD-810 were absolutely calibrated for protons. The nature of the acceleration mechanism to map surface structure in a high resolution film detector enables a full characterization of beam parameter within a single shot.

The beam reconstruction method delivers a decreasing full angle of beam spread for increasing proton energy of 35°–4° (TRIDENT), 42°–10° (100TW-LULI), and 62°–15° (VULCAN). A Lorentzian reflects the real source size behavior best with a FWHM of 44 μm for TRIDENT, 56 μm for 100TW-LULI, and 240 μm for VULCAN. The position of the virtual source size in front of the target is energy dependent and is for all laser systems between (30–125) μm. The factor of 5 higher obtained with the Vulcan laser could result from the high laser pulse energy. Further investigation is required. The diameter of the virtual source size is decreasing from 5 to 3 μm for increasing proton energy, and for VULCAN it is around 12 μm. The normalized transverse emittances of the proton beams calculated with the ellipse
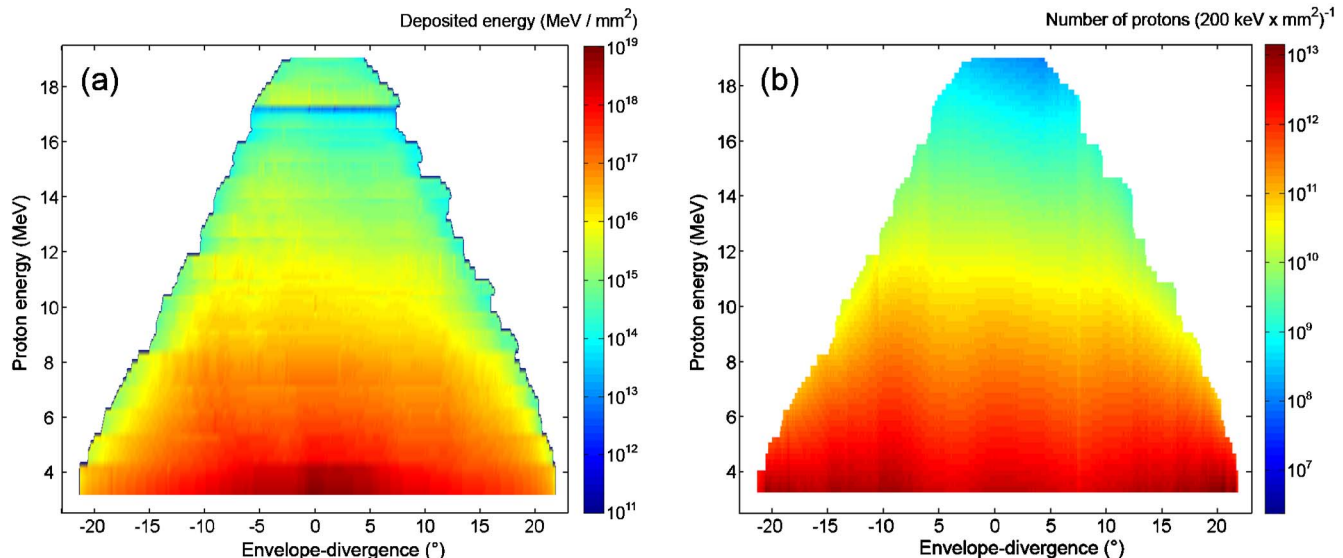

FIG. 13. (Color online) (a) Reconstructed total deposited energy distribution for the TRIDENT proton beam (after subtraction). The film type change from HD-810 to MD-55 at 17 MeV is clearly visible. (b) Spatial and energy resolved proton spectrum for the TRIDENT shot. The particle number is given for an energy interval of 200 keV, the same interval resolution as in the described algorithm for the gap between two layers.
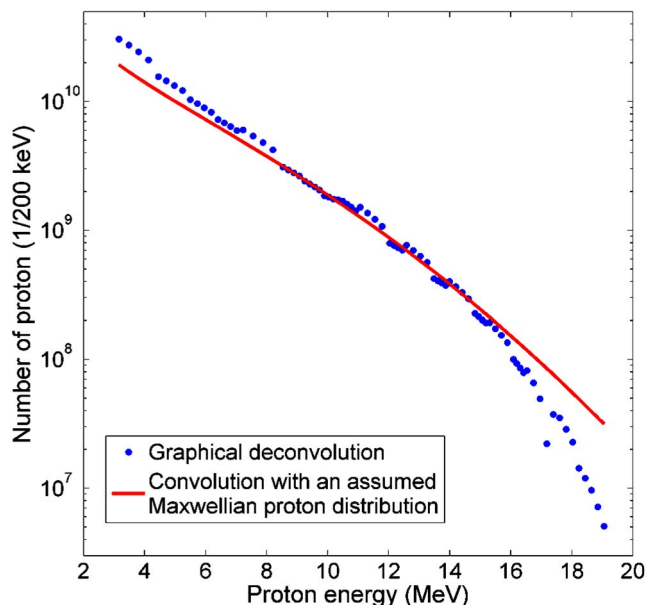
FIG. 14. (Color online) The comparison of the proton distribution function obtained by the analytical deconvolution (Sec. IV E) and the developed method of the graphical subtraction. The proton number is given for an energy interval of 200 keV. This size is consistent with the energy interval between two layers in the graphical subtraction. The agreement of the measurement and the fit confirms the use of a Maxwellian proton distribution as a feasible approximation for the spectrum.

tained can also be used for the validation of acceleration models. RCF imaging spectroscopy provides a basis for proton beam scaling measurements.

approximation are below 0.3π mm mrad, for VULCAN slightly higher, and decreasing for increasing proton energy (upper limits). The influence of nonlinear forces on laser-accelerated proton beams can be shown in the phase-space illustration, and it points out that different area approximations are too inaccurate resulting in incorrect data interpretation. The rms emittances are of the same order of magnitude lower than the ellipse values, but laser-accelerated proton beams still show divergences from the uniform case. It has been shown that the measurement of the RCF imaging spectroscopy worked very well at all laser systems and that this method can be a tool to characterize a laser system with respect to its proton-acceleration capability. In addition an algorithm to calculate the spatial and energy resolved proton distribution has been developed and tested to get a better picture of the spatial distribution of laser-accelerated proton beams. The conformity of the analytical and the graphical method to obtain the deconvolved proton distribution approves the use of a Maxwellian proton distribution as a feasible approximation for the spectrum. Knowledge on the spatial information of the energy deposition of such beams is essential for further applications of these laser-accelerated proton beams.

The results obtained in this work are useful for the full characterization of laser-accelerated proton beams. For applications such as, e.g., proton radiography, proton fast ignition in medicine, or laser-accelerated proton beams as a novel particle source for conventional accelerator structures, it is indispensable to know these important beam parameters. This measurement technique can be used to control beam optimization by target or laser modification. The data ob-

[1] A. P. Fews, P. A. Norreys, F. N. Beg, A. R. Bell, A. E. Dangor, C. N. Danson, P. Lee, and S. J. Rose, Phys. Rev. Lett. **73**, 1801 (1994).
[2] A. Maksimchuk, S. Gu, K. Flippo, D. Umstadter, and V. Yu. Bychenkov, Phys. Rev. Lett. **84**, 4108 (2000).
[3] E. L. Clark, K. Krushelnick, J. R. Davis, M. Zepf, M. Tatarakis, F. N. Beg, A. Machacek, P. A. Norreys, M. I. K. Santala, I. Watts, and A. E. Dangor, Phys. Rev. Lett. **84**, 670 (2000).
[4] R. A. Snavely, M. H. Key, S. P. Hatchett, T. E. Cowan, M. Roth, T. W. Phillips, M. A. Stoyer, E. A. Henry, T. C. Sangster, M. S. Singh, S. C. Wilks, A. MacKinnon, A. Offenberger, D. M. Pennington, K. Yasuike, A. B. Langdon, B. F. Lasinski, J. Johnson, M. D. Perry, and E. M. Cambell, Phys. Rev. Lett. **85**, 2945 (2000).
[5] S. P. Hatchett, P. Hatchett, C. G. Brown, T. E. Cowan, E. A. Henry, J. S. Johnson, M. H. Key, J. A. Koch, A. B. Langdon, B. F. Lasinski, R. W. Lee, A. J. Mackinnon, D. M. Pennington, M. D. Perry, T. W. Phillips, M. Roth, T. C. Sangster, M. S. Singh, R. A. Snavely, M. A. Stoyer, S. C. Wilks, and K. Yasuike, Phys. Plasmas **7**, 2076 (2000).
[6] A. J. Mackinnon, M. Borghesi, S. Hatchett, M. H. Key, P. K. Patel, H. Campbell, A. Schiavi, R. Snavely, S. C. Wilks, and O. Willi, Phys. Rev. Lett. **86**, 1769 (2001).
[7] L. Robson, P. T. Simpson, P. McKenna, K. W. D. Ledingham, R. J. Clarke, T. McCanny, D. Neely, O. Lundh, F. Lindau, C.-G. Wahlström, and M. Zepf, Nat. Phys. **3**, 58 (2007).
[8] T. Cowan, J. Fuchs, H. Ruhl, A. Kemp, P. Audebert, M. Roth, R. Stephens, I. Barton, A. Blažević, E. Brambrink, J. Cobble, J. Fernandez, J.-C. Gauthier, M. Geissel, M. Hegelich, J. Kaae, S. Karsch, G. P. Le Sage, S. Letzring, M. Manclossi, A. Newkirk, H. Pepin, and N. Renard-LeGalloudec, Phys. Rev. Lett. **92**, 204801 (2004).
[9] E. Brambrink, J. Schreiber, T. Schlegel, P. Audebert, J. Cobble, J. Fuchs, B. M. Hegelich, and M. Roth, Phys. Rev. Lett. **96**, 154801 (2006).
[10] K. Flippo, B. M. Hegelich, B. J. Albright, L. Yin, D. C. Gautier, S. Letzring, M. Schollmeier, J. Schreiber, R. Schulze, and J. C. Fernandez, Laser Part. Beams **25**, 3 (2007).
[11] I. Spencer, K. W. D. Ledingham, R. P. Singhal, T. McCanny, P. McKenna, E. L. Clark, K. Krushelnick, M. Zepf, F. N. Beg, M. Tatarakis, A. E. Dangor, P. A. Norreys, R. J. Clarke, R. M. Allott, and I. N. Ross, Nucl. Instrum. Methods Phys. Res. B **183**, 449 (2001).
[12] V. Malka, S. Fritzler, E. Lefebvre, E. d'Humieres, R. Ferrand, G. Grillon, C. Albaret, S. Meyroneinc, J.-P. Chambaret, A. Antonetti, and D. Hulin, Med. Phys. **31**, 1587 (2004).
[13] M. Borghesi, D. H. Campbell, A. Schiavi, O. Willi, A. J. Mackinnon, D. Hicks, P. Patel, L. A. Gizzi, M. Galimberti, and R. J. Clarke, Laser Part. Beams **20**, 269 (2002).
[14] K. Krushelnick, E. L. Clark, R. Allott, F. N. Beg, C. N. Danson, A. Machacek, V. Malka, Z. Najmudin, D. Neely, P. A. Norreys, M. R. Salvati, M. I. K. Santala, M. Tatarakis, I. Watts, M. Zepf, and A. E. Dangor, IEEE Trans. Plasma Sci. **28**, 1184 (2000).
[15] M. Schollmeier, S. Becker, M. Geißel, K. A. Flippo, A. Blažević, S. A. Gaillard, D. C. Gautier, F. Grüner, K. Harres, M. Kimmel, F. Nürnberg, P.

Rambo, U. Schramm, J. Schreiber, J. Schütrumpf, J. Schwarz, N. A. Tahir, B. Atherton, D. Habs, B. M. Hegelich, and M. Roth, Phys. Rev. Lett. **101**, 055004 (2008).

[16] M. Roth, T. E. Cowan, M. H. Key, S. P. Hatchett, C. Brown, W. Fountain, J. Johnson, D. M. Pennington, R. A. Snavely, S. C. Wilks, K. Yasuike, H. Ruhl, F. Pegoraro, S. V. Bulanov, E. M. Campbell, M. D. Perry, and H. Powell, Phys. Rev. Lett. **86**, 436 (2001).

[17] P. Mora, Phys. Rev. Lett. **90**, 185002 (2003).

[18] S. C. Wilks, A. B. Langdon, T. E. Cowan, M. Roth, M. Singh, S. Hatchett, M. H. Key, D. Pennington, A. MacKinnon, and R. A. Snavely, Phys. Plasmas **8**, 542 (2001).

[19] A. J. Kemp, J. Fuchs, Y. Sentoku, V. Sotnikov, M. Bakeman, P. Antici, and T. E. Cowan, Phys. Rev. E **75**, 056401 (2007).

[20] S. Karsch, S. Düsterer, H. Schwoerer, F. Ewald, D. Habs, M. Hegelich, G. Pretzler, A. Pukhov, K. Witte, and R. Sauerbrey, Phys. Rev. Lett. **91**, 015001 (2003).

[21] J. Fuchs, Y. Sentoku, S. Karsch, J. Cobble, P. Audebert, A. Kemp, A. Nikroo, P. Antici, E. Brambrink, A. Blažević, E. M. Campbell, J. C. Fernandez, J.-C. Gauthier, M. Geissel, M. Hegelich, H. Pepin, H. Popescu, N. Renard-LeGalloudec, M. Roth, J. Schreiber, R. Stephens, and T. E. Cowan, Phys. Rev. Lett. **94**, 045004 (2005).

[22] Y. Sentoku, K. Mima, P. Kaw, and K. Nishikawa, Phys. Rev. Lett. **90**, 155001 (2003).

[23] H. Schwoerer, S. Pfotenhauer, O. Jäckel, K.-U. Amthor, B. Liesfeld, W. Ziegler, R. Sauerbrey, K. W. D. Ledingham, and T. Esirkepov, Nature (London) **439**, 445 (2006).

[24] B. M. Hegelich, B. J. Albright, J. Cobble, K. Flippo, S. Letzring, M. Paffett, H. Ruhl, J. Schreiber, R. K. Schulze, and J. C. Fernández, Nature (London) **439**, 441 (2006).

[25] H. Ruhl, T. E. Cowan, and J. Fuchs, Phys. Plasmas **11**, L17 (2004).

[26] M. Roth, A. Blažević, M. Geissel, T. Schlegel, T. E. Cowan, M. Allen, J.-C. Gauthier, P. Audebert, J. Fuchs, J. Meyer-ter-Vehn, M. Hegelich, S. Karsch, and A. Pukhov, Phys. Rev. ST Accel. Beams **5**, 061301 (2002).

[27] GafChromic radiochromic film types HD-810, HS, MD-55; ISP Corporation, Wayne, New Jersey 07470, USA, http://www.ispcorp.com/products/dosimetry/ (2008).

[28] W. L. McLaughlin, M. Al-Sheikhly, D. F. Lewis, A. Kovacs, and L. Wojnarovits, *Radiochromic Solid-State Polymerization Reaction*, Chap. 11 in: R. L. Clough and S. W. Shalaby, Irradiation of Polymers (American Chemical Society, Washington, DC, 1996).

[29] D. S. Hey, M. H. Key, A. J. Mackinnon, A. G. MacPhee, P. K. Patel, R. R. Freeman, L. D. Van Woerkom, and C. M. Castaneda, Rev. Sci. Instrum. **79**, 053501 (2008).

[30] A. Niroomand-Rad, C. R. Blackwell, B. M. Coursey, K. P. Gall, J. M. Galvin, W. L. McLaughlin, A. S. Meigooni, R. Nath, J. E. Rodgers, and C. G. Soares, Med. Phys. **25**, 2093 (1998).

[31] H. Alva, H. Mercado-Uribe, M. Rodriguez-Villafuerte, and M. E. Brandan, Phys. Med. Biol. **47**, 2925 (2002).

[32] Grey wedge #T4110cc, Stouffer Graphic Arts, Mishawaka, IN 46544, USA; 41 Steps from Optical Density 1 to 4, http://www.stouffer.net (2008).

[33] J. F. Ziegler, J. P. Biersack, and U. Littmark, *The Stopping and Range of Ions in Solids* (Pergamon, New York, 1985).

[34] A. Z. Jones, C. D. Bloch, E. R. Hall, R. Hashemian, S. B. Klein, B. von Przewoski, K. M. Murray and C. C. Foster, IEEE Trans. Nucl. Sci. **46**, 1762 (1999).

[35] S. Humphries, Jr., *Charged Particle Beams* (Wiley, New York, 1990).

[36] F. M. Bieniosek, L. R. Prost, P. A. Seidl, A. W. Molvik, and M. Kireeff Covo, Nucl. Instrum. Methods Phys. Res. A **544**, 268 (2005).

[37] J. Fuchs, Y. Sentoku, E. d'Humieres, T. E. Cowan, J. Cobble, P. Audebert, A. Kemp, A. Nikroo, P. Antici, E. Brambrink, A. Blažević, E. M. Campbell, J. C. Fernandez, J.-C. Gauthier, M. Geissel, M. Hegelich, S. Karsch, H. Popescu, N. Renard-LeGalloudec, M. Roth, J. Schreiber, R. Stephens, and H. Pepin, Phys. Plasmas **14**, 053105 (2007).

[38] P. M. Lapostolle, IEEE Trans. Nucl. Sci. **18**, 1101 (1971).

[39] M. Reiser, *Theory and Design of Charged Particle Beams* (Wiley, Albuquerque, NM, 1994).

[40] J. Fuchs, P. Antici, E. D. Humieres, E. Lefebvre, M. Borghesi, E. Brambrink, C. A. Cecchetti, M. Kaluza, V. Malka, M. Manclossi, S. Meyroneinc, P. Mora, J. Schreiber, T. Toncian, H. Pepin, and P. Audebert, Nat. Phys. **2**, 48 (2006).

[41] P. Mora, Phys. Rev. E **72**, 056401 (2005).

[42] J. Fuchs, C. A. Cecchetti, M. Borghesi, T. Grismayer, E. d'Humieres, P. Antici, S. Atzeni, P. Mora, A. Pipahl, L. Romagnani, A. Schiavi, Y. Sentoku, T. Toncian, P. Audebert, and O. Willi, Phys. Rev. Lett. **99**, 015002 (2007).

[43] J. J. Thomson, Philos. Mag. **21**, 225 (1911).

[44] K. Harres, M. Schollmeier, E. Brambrink, P. Audebert, A. Blažević, K. Flippo, D. C. Gautier, M. Geißel, B. M. Hegelich, F. Nürnberg, J. Schreiber, H. Wahl, and M. Roth, Rev. Sci. Instrum. **79**, 093306 (2008).

[45] B. Dromey, S. Kar, P. Foster, and M. Zepf, Rev. Sci. Instrum. **75**, 645 (2004).

[46] A. P. Fews, Nucl. Instrum. Methods Phys. Res. B **71**, 465 (1992).

[47] M. Borghesi, A. J. Mackinnon, D. H. Campbell, D. G. Hicks, S. Kar, P. K. Patel, D. Price, L. Romagnani, A. Schiavi, and O. Willi, Phys. Rev. Lett. **92**, 055003 (2004).

[48] Injector group, GSI Helmholtzzentrum für Schwerionenforschung, Darmstadt, Germany, www-inj.gsi.de (2007).

[49] T. Winkelmann, R. Cee, T. Haberer, A. Naas, A. Peters, S. Scheloske, P. Spädtke, and K. Tinschert, Rev. Sci. Instrum. **79**, 02A331 (2008).

[50] E. Breschi, M. Borghesi, M. Galimberti, D. Giuliettia, L. A. Gizzia, and L. Romagnani, Laser Part. Beams **22**, 393 (2004).